Ultramicroscopy 153 (2015) 45–54

Contents lists available at ScienceDirect

Ultramicroscopy

journal homepage: www.elsevier.com/locate/ultramic

On the capability of in-situ exposure in an environmental scanning electron microscope for investigating the atmospheric corrosion of magnesium

M. Esmaily [a,*], N. Mortazavi [b], M. Shahabi-Navid [a], J.E. Svensson [a], L.G. Johansson [a], M. Halvarsson [b]

[a] Department of Chemical and Biological Engineering, Chalmers University of Technology, SE-412 96 Gothenburg, Sweden
[b] Department of Applied Physics, Chalmers University of Technology, SE-412 96 Gothenburg, Sweden

ARTICLE INFO

Article history:
Received 18 November 2014
Received in revised form
19 February 2015
Accepted 21 February 2015
Available online 23 February 2015

Keywords:
In-situ microscopy
ESEM
Chamber pressure
Atmospheric corrosion

ABSTRACT

The feasibility of environmental scanning electron microscope (ESEM) in studying the atmospheric corrosion behavior of 99.97% Mg was investigated. For reference, ex-situ exposure was performed. A model system was designed by spraying few salt particles on the metal surface and further promoting the corrosion process using platinum (Pt) deposition in the form of $1 \times 1 \times 1\ \mu m^3$ dots around the salt particles to create strong artificial cathodic sites. The results showed that the electron beam play a significant role in the corrosion process of scanned regions. This was attributed to the irradiation damage occurring on the metal surface during the ESEM in-situ experiment. After achieving to a reliable process route, in a successful attempt, the morphology and composition of the corrosion products formed in-situ in the ESEM were in agreement with those of the sample exposed ex-situ.

1. Introduction

Environmental scanning electron microscopy (ESEM) has established itself as a promising method for studying the interaction of different materials with humid air or water in different disciplines such as geology, medicine, biology, life and food science [1–3]. However, the use of ESEM in materials science research has been delayed for much time. This is due to the essential needs and considerations in preparation techniques and the problems associated with the pressure inside the microscope chamber. A practical example of potential uses of ESEM is the atmospheric corrosion of metals, where there is an interaction of metal surface with the micro-droplets, the transition of micro-droplets to an electrolyte layer, and then the formation of corrosion products on the metal surface [4–9]. In this regard, the ESEM method is expected to provide useful information on the early stages of corrosion, which will have an impact on the later stages of a corrosion process. Although the initial stages of the corrosion process can be investigated ex-situ using well-controlled corrosion chambers and field exposures [6–11], the problem with this approach is that the dynamic phenomena in the corrosion process, including the formation of the electrolyte layer and corrosion products cannot be monitored as it occurs. In-situ exposure within an ESEM can be considered as a powerful tool to investigate the very initial stages of corrosion "live". The localized and electrochemical nature and relatively fast kinetics of NaCl-induced atmospheric corrosion of some metallic materials such as magnesium (Mg) and Mg alloys imply that it would be possible to study the atmospheric corrosion by in-situ microscopy.

In the ESEM, the state of hydration of the specimen is determined by its temperature and the water vapor pressure in the microscope chamber [2,3]. Thus, ESEM can provide a combination of the required aggressive environment and continuous imaging throughout the corrosion process. This combination gives a unique opportunity to investigate the initiation and growth processes of the corrosion products on different metal grains. There are few in-situ ESEM corrosion studies on Mg and Mg alloys available in the literature [12–16]. Chen et al. [14] investigated the corrosion behavior of Mg alloys by changing the RH of the ESEM chamber. They examined the corrosion of the alloy AZ91 at a fixed value of RH in wet and dry cycles to study the effect of process parameters on corrosion product formation. Rossi et al. [16] studied initial stages of the NaCl-induced corrosion process on the surface of pure zinc (Zn) and Mg by means of ESEM using a humidostatic chamber. They promoted the corrosion process by increasing the RH of the

* Corresponding author.
E-mail address: mohsen.esmaily@chalmers.se (M. Esmaily).

http://dx.doi.org/10.1016/j.ultramic.2015.02.010

ESEM chamber and claimed that the ESEM could simulate an aggressive environment.

The ESEM method has also been successfully employed for oxidation experiments on steels and ceramics at high temperatures [17–20]. Jonsson et al. [20], who studied the initial oxidation of low-alloyed steel in the presence of small amounts of KCl (s) through ESEM in-situ exposure, stated that the in-situ results were in good agreement with corresponding tube furnace exposures in terms of the composition, thickness and morphology of the oxide scale. Despite of these attempts, still, there is a need to understand the effect the lower exposure pressure (~2–4 Torr) and the presence of an electron beam (e-beam) on the corrosion mechanisms occurring in the ESEM. The atmospheric corrosion behavior of Mg and Mg alloys under outdoor conditions and in the laboratory has been extensively investigated [21–26]. In this study, the influence of the two mentioned inherent parameters of the ESEM in-situ exposure on the NaCl-induced atmospheric corrosion process of pure Mg was examined. The corrosion mechanism inside the ESEM chamber was described and the results were compared to those of the ex-situ exposures.

2. Experimental

Pure Mg (99.97% Mg) with a chemical composition of 0.005% Zn, 0.003% Al, 0.003% Si, 0.0023% Mn and 0.001% Fe and balance Mg (by weight) was used as the test material. The in-situ exposures were performed by means of a FEI Quanta 200 FEG ESEM (FEI Company, Hillsboro, OR, USA) with a Schottky Field Emission Gun (FEG). We used an oil free pump to prevent carbonaceous depositions over the scanned areas. Imaging was performed throughout the degradation process using an acceleration voltage of 20–30 kV. The instrument was equipped with Oxford Inca energy dispersive X-ray detector (EDX).

Post-exposure analyses were performed by SEM/EDX for local chemical composition analysis of the corrosion products as well as elemental mapping of corroded metal surfaces. Samples were machined from ingot to obtain small-sized cylinders with dimensions of 3 mm diameter and 4 mm height according to the required dimension for placing the samples inside the Peltier heating/cooling stage for the ESEM in-situ experiments, see Fig. 1. The Peltier stage enables operating exposures in temperature between –20 and 100 °C [2]. In this study a temperature of 4 °C was used for the in-situ exposures, see below. Prior to corrosion

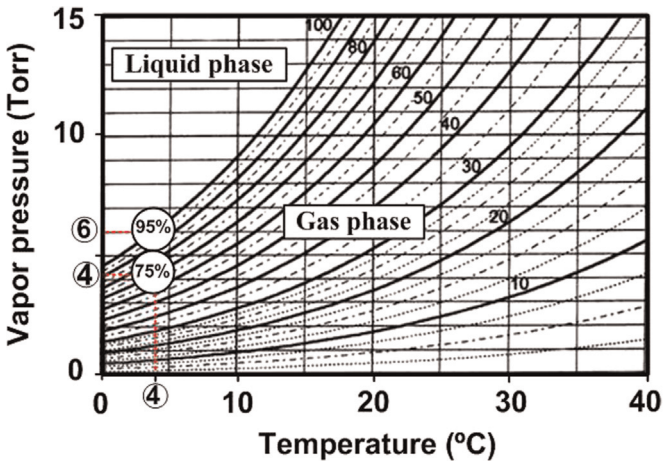

Fig. 2. Relative humidity (RH) isobar [10] chart used for the in-situ corrosion experiment. Showing the temperature and pressure used for the in-situ experiments to produce relative humidity (RH) of 75% and 95%.

experiments, a solution of 20 ml distilled water, 80 ml ethanol and 1 g NaCl was sprayed on the samples, which in total were contaminated with 5 μg/cm^2 NaCl (equal to 40 μg Cl^- C m^{2-} y^{-1} salt).

In ESEM, water can be condensed on a sample surface by decreasing the Peltier cooling stage temperature to *few degrees* and increasing the chamber pressure. The liquid/gas phase border is 6.1 Torr at 4 °C according to the relative humidity (RH) isobar shown in Fig. 2. Hence, a higher pressure than 6.1 Torr will result in liquid condensation (100% RH) on the metal surface, while using a lower pressure controls the RH in the gas phase (< 100% RH). As local analyses were performing in individual grains, it was essential to identify the crystallographic orientation of the grains studied before the exposures. This was done using a LEO Ultra 55 FEG-SEM equipped with an HKL Channel 5 Electron Backscatter Diffraction (EBSD) system. The sample preparation procedure for the EBSD measurement is described elsewhere [27].

The exposures performed in this study are explained in Table 1. Three ESEM in-situ exposures were performed at two different RH (75% and 95%). Different levels of RH were used to observe the formation of the electrolyte layer in different humid environments. The exposures time and temperature were 320 min (5 h) and 4 °C, respectively. Different RH vales were obtained by employing different chamber pressures, see Fig. 2.

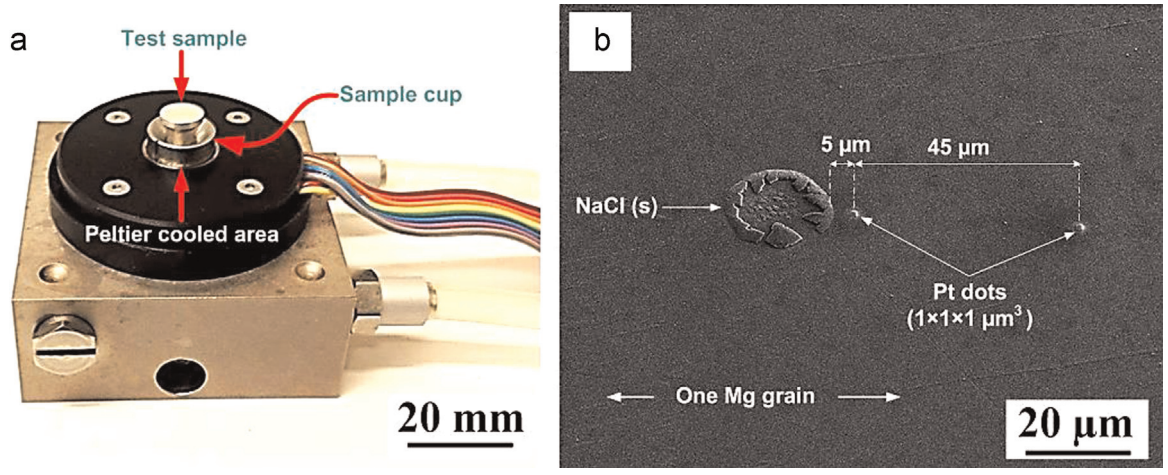

Fig. 1. (a) Photo of the Peltier cooling stage of the FEI Quanta 200 FEG ESEM used in this study and (b) SE SEM image showing the position of the two Pt spots with respect to the salt droplet.

Table 1
Description of the exposures performed in this study.

	Descripting
1st Exposure	ESEM in-situ exposure at 75% RH for 320 min. No Pt was deposited on the sample.
2nd Exposure	ESEM in-situ exposure at 95% RH for 320 min. Two regions containing NaCl(s)+Pt dots. One situated under the e-beam and one far away (4 mm) from the e-beam.
3rd Exposure	ESEM in-situ exposure; the sample and exposure conditions were the same as the second exposure. Right before the experiment, ESEM chamber and the sample were cleaned using isopropanol and plasma cleaner, respectively.
In desiccator	Ex-situ exposure in a hermetically closed desiccator, performing the exposure at 95% RH by equilibrating air with 500 ml potassium hydroxide solution (KOH(aq)).

The investigations were centered around the samples exposed at 95% RH (the second and third exposures) and focused on two salted-regions, one under electron beam (the e-beam effect) and the other one 4 mm further away from the location of e-beam (the pressure effect). To additionally accelerate the corrosion process two platinum (Pt) dots with a dimension of $1 \times 1 \times 1\ \mu m^3$ were deposited around the salt crystals, one dot at a distance of 4 μm and the other one deposited at a distance of 50 μm from the salt particles, as shown in Fig. 2. The Pt depositions were done using an FEI Versa 3D Focused Ion Beam/SEM (FIB/SEM) workstation that is a dual beam system, equipped with both an electron and an ion column.

In addition, the in-situ exposure was simulated using a hermetically closed desiccator to evaluate the effect of lower pressure on the corrosion process inside the ESEM. The desiccator (as a corrosion reactor) exposure enabled us to perform exposure in the absence of CO_2 similar to the ESEM in-situ exposure condition. Exposure temperature was similar to that of the in-situ exposure, i.e. 4 °C. 95% RH was achieved by equilibrating the air with 500 ml potassium hydroxide solution (KOH(aq)) that was poured in a container placed inside the desiccator. The water vapor partial pressure over KOH(aq) was calculated by the following equation [28]:

$$\log p_{w\,(KOH)} = -0.01m - 0.001m^2 + 2.258 \times 10^{-5}m^3 + (1 - 0.001m + 5.602 \times 10^{-4}m^2 - 7.822 \times 10^{-6}m^3) \times (35.446 - 3343446 - 3343.93/T - 10.9\log T + 0.01T)\ (\text{bar}) \quad (1)$$

where P_w is the equilibrium partial pressure of water vapor over the aqueous solution, m is the molality and T is the experiment temperature. In addition to regulating the RH to the desired value, i.e. 95% RH, the KOH(aq) solution also functioned as a CO_2 absorbent.

3. Results

The series of images in Fig. 3 show the initial stages of atmospheric corrosion of pure Mg in the first experiment, i.e. the in-situ exposure at 75% RH (T: 4 °C, P: 4 Torr) for 320 min. In this

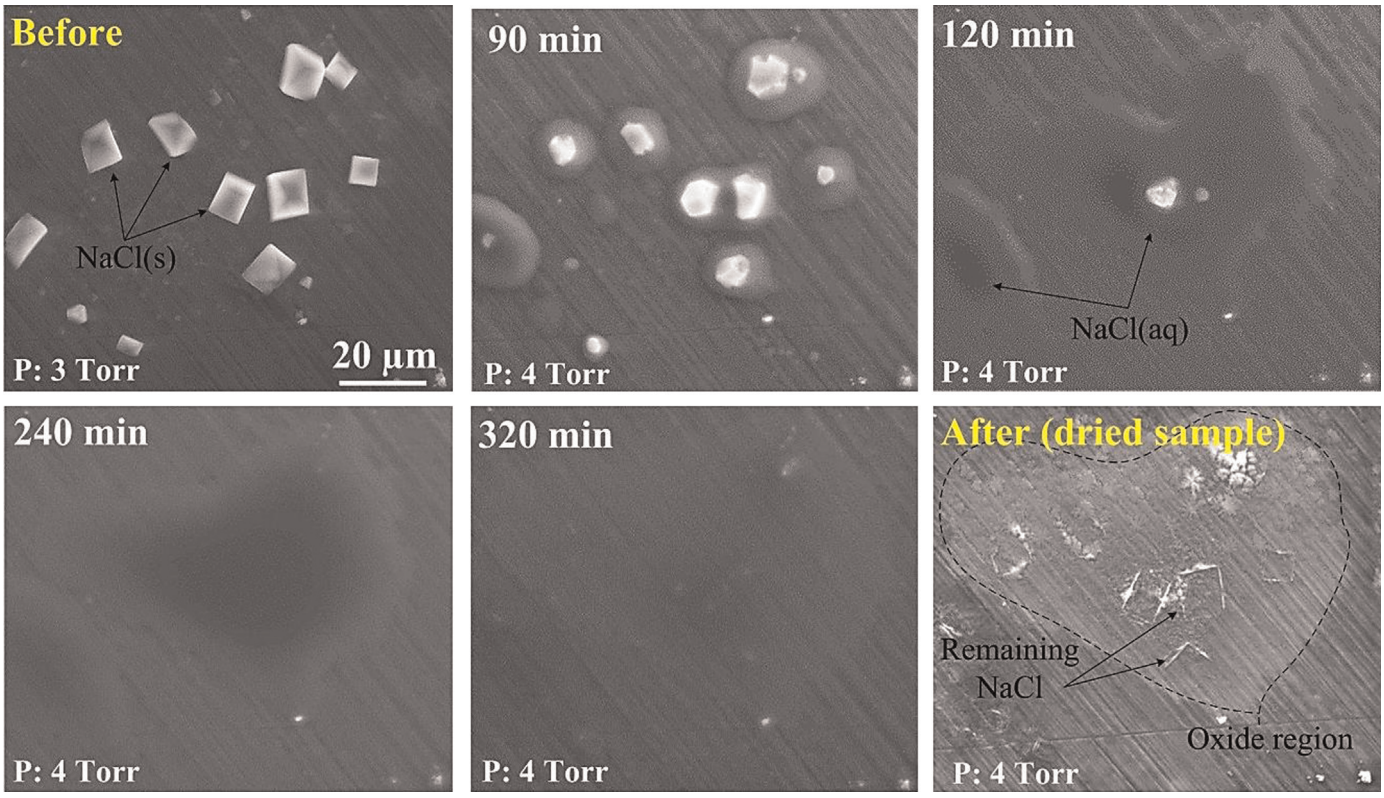

Fig. 3. ESEM micrographs of the corrosion progress in 99.97% Mg at 75% RH and 4 °C (the first ESEM exposure).

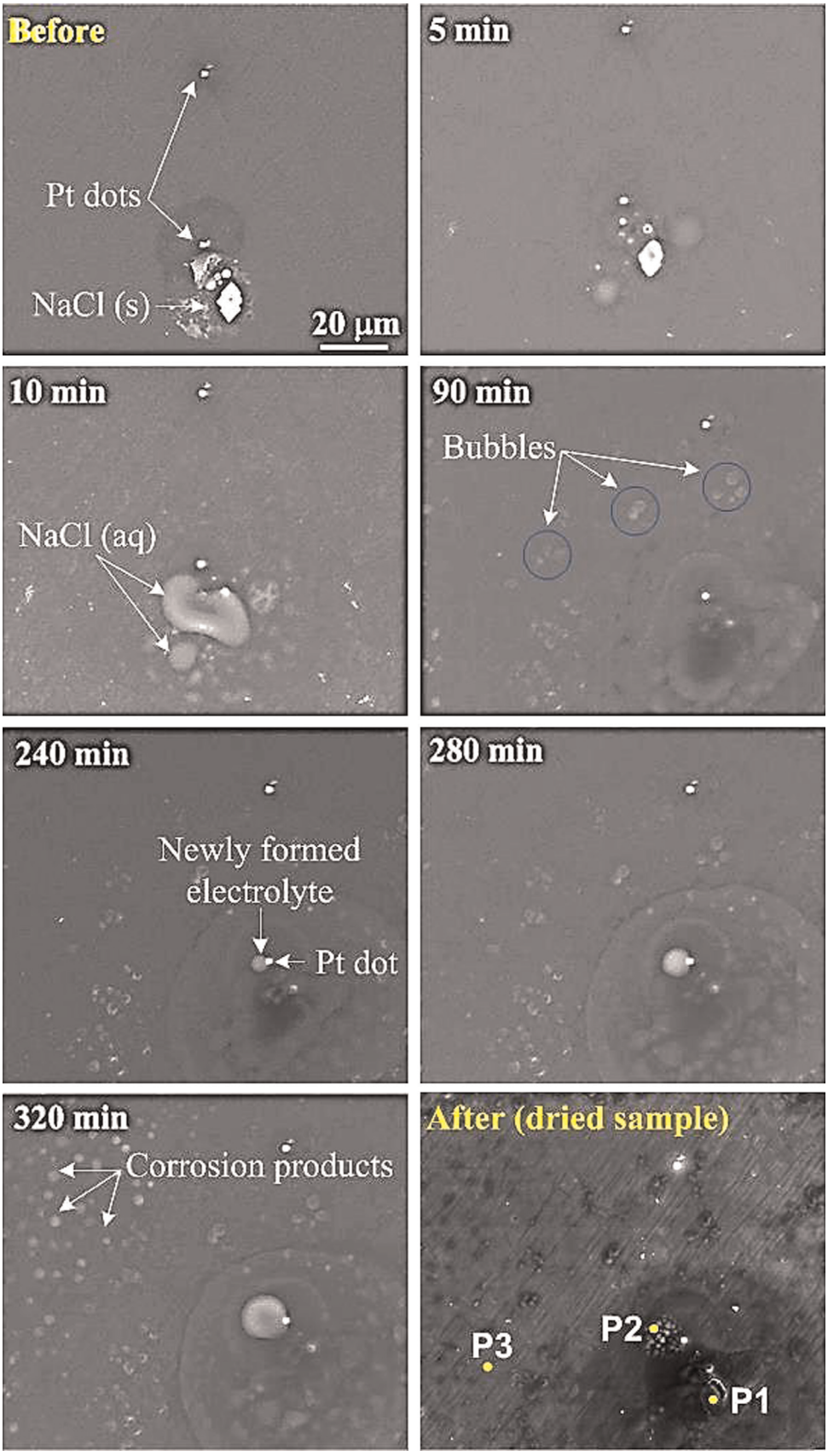

Fig. 4. ESEM micrographs of the corrosion progress in pure Mg at 4 °C and a pressure of 6 Torr (the second ESEM exposure). The chemical composition of P1, P2 and P3 are listed in Table 2.

exposure, no Pt was deposited and the sample was just contaminated with NaCl(s) particles, as explained in Table 1. The microscope chamber pressure was initially set to 1 Torr, corresponding to a RH value of about 20%. As this was well below the critical humidity level required to form a NaCl(aq), microscopic imaging showed no changes on the sample surface compared to the dry case. We increased the chamber pressure to 4 Torr H_2O (corresponding 75% RH). After 90 min exposure at 75% RH, the corrosion process was slowly initiated. NaCl crystallites were observed to slowly convert onto the liquid phase. After 120 min, most of the salt crystallites were in the form of NaCl(aq). It was noticed that, the conversion process was finished after 240 min. The deliquescence of NaCl was accompanied by the formation of corrosion products in association with the salt solution droplets. After more than 320 min exposure, the pressure was lowered and accordingly water was evaporated. The remaining (unconsumed) NaCl(aq) recrystallized on the metal surface. Seemingly, no voluminous corrosion product was observed on the sample surface. The edges of the former large salt crystals were also visible in the "after" ESEM image in Fig. 3.

Fig. 4 shows sequence of the in-situ corrosion process in the second exposure inside the ESEM, exposure at 95% RH (T: 4 °C, P: 6 Torr) for up to 320 min wetting period. As described in Table 1, this exposure was performed on the sample that was contaminated by both NaCl and Pt dots, acting as corrosion accelerators. In this case, the corrosion process was slowly initiated after 5 min exposure time by the conversion of NaCl particles to the electrolyte layer (NaCl(aq)). It may be noted that this is in a clear contrast with the first exposure (75% RH), where the liquid phase was started to form after 90 min wetting. After 10 min, the salt particles were fully converted onto the liquid phase. It was interesting to observe that bubbles started to generate all over the Mg surface. These bubbles are likely due to the hydrogen evolution produced by the cathodic reduction of water [12]. Thus, there was a clear difference in the kinetic of the corrosion process in the first (75% RH) and the second (95% RH) in-situ exposures.

A distinct electrolyte film started to form in the vicinity of the Pt dot/NaCl(aq) after 240 min exposure time. The electrolyte grew with wetting time; compare the ESEM images after 240 and 320 min in Fig. 4. A corrosion crust was observed on the same regions after 24 h (dried sample). The chemical compositions of the marked points (P1, P2 and P3) are listed in Table 2. P1, which shows the composition of the corrosion crust, contained Mg, carbon (C) and oxygen (O). It was clear that the C content of the corrosion product, i.e. P1, with a value of 50 wt%, was unexpectedly high. P2 shows the chemical composition of the region in vicinity of the Pt dot. The EDX results indicated that this area was highly enriched in sodium (Na) and poor in chlorine (Cl). The chemical composition of P3, which is taken far away from the corrosion cell and on the metal surface, can be considered as another indication of high C content on the corroded metal surface.

Table 2
Chemical composition (wt%) analyses of the second in-situ exposure, points marked in Figs. 4 and 6.

	Under e-beam (Fig. 3)			**No e-beam** (Fig. 6)		
	P1	P2	P3	P4	P5	P6
Mg	34.8 ± 0.3	25.2 ± 0.6	85.4 ± 1.5	38 ± 0.5	26 ± 0.9	91.7 ± 1.9
O	13.54 ± 1.2	34.1 ± 3.7	2.6 ± 0.23	52.96 ± 3.7	34 ± 1.2	2.3 ± 0.2
C	50 ± 4.2	12.8 ± 2.5	12 ± 1.9	12 ± 1.2	9.1 ± 2.1	6 ± 1.5
Na	1.57 ± 0.2	27.9 ± 4.2	–	–	30.9 ± 3.2	–
Cl	0.09[a]	–	–	0.04[a]	–	–

[a] The scatter for these cases were negligible (< ± 0.1).

Two low-magnification SEM images from the same sample but after the exposure are presented in Fig. 5. The attention is drawn to the scanned region that was highly affected by e-beam during the 320 min continuous imaging process. It seemed that the extent of corrosion attack was remarkably less in the region that was under the e-beam compared to the non-scanned area.

Fig. 6 presents the corrosion morphology and EDX elemental mapping for Mg, O, C, Na, Cl and Pt acquired from the second region that was not under the e-beam (but contained salt and Pt dots). Worm-like corrosion crust was observed and grew from the former location of the salt particle/Pt dot, see for e.g. Fig. 6. The EDX maps show that the corrosion products were dominated by Mg, O and C. Na was accumulated in the vicinity of the Pt dot. The Pt dots can be seen in the SE image and in the Pt map. No Cl was detected on corrosion crusts and other regions in the metal surface. The EDX point analyses of P4, P5 and P6, given in Table 2, implied that the C content of the corrosion product for this region was less than that of the region that was under the e-beam.

The ex-situ experiment was performed in the absence of CO_2, for comparing the results with those of the ESEM exposures. Fig. 7 shows SEM images of the corroded Mg exposed in the desiccator for 320 min. The micrographs clearly showed that the extent of corrosion attack varied significantly from one region to another and largely depended on the features (NaCl particles and Pt dots) that were present on the metal surface. The unreacted salt crystallites (in the low-mag SEM image in Fig. 7a) corresponded to NaCl(aq) solution present on the metal surface at the end of the exposure and recrystallized upon drying.

The most important observations made were as follows: (i) the formation of small corrosion nodules in the metal surface; (ii) a more severe corrosion attack in the location of the salt droplets; (iii) no or very little evidence for corrosion in the vicinity of Pt dots and where the salt particle was absent; (iv) a mild corrosion attack where only salt (and no Pt) was present in the metal surface as unconsumed dendritic NaCl crystals was detected (see the low magnification SEM image Fig. 7a); and (v) the most severe corrosion attack on the metal surface in regions where both salt and Pt dot were present (Fig. 7a and b).

In some cases the corrosion morphology developed as corrosion product accumulations by forming elongated "worm-like" features, see Fig. 7a, similar to the corrosion morphologies observed in the sample exposed in-situ (SE image in Fig. 7). Otherwise, semicircular corrosion crusts (Fig. 7b) were observed, similar to that formed on the sample exposed in-situ (see the dried case in Fig. 4). The chemical compositions of the points marked in Fig. 7b indicated the presence of the cathodic and anodic sites on the metal surface. The primary elements contained in the corrosion products (anodic region) were O, Mg and C with a minor trace amount of Cl and Na. The surrounding region of the Pt spot was highly enriched in Na. The scare evidence of Cl on the corroded surface as well as high Na content around the Pt dots were in excellent agreement with those of the in-situ experiment. However, as expected, there was a considerable difference in the C content of the corrosion products formed by ex-situ exposure compared to that of the in-situ ESEM experiment.

The higher C content of the corrosion products formed in-situ inside the ESEM compared to that of ex-situ was somehow surprising as the CO_2 concentration is not more than few parts per million (ppm) owing to the purging process (pumping) of the ESEM chamber. Therefore, to tackle this problem and successfully simulate the ex-situ exposure, the third in-situ exposure was performed by eliminating the carbon sources inside the ESEM chamber. Accordingly, the sample was cleaned by plasma cleaning prior to the next in-situ exposure. Additionally, the ESEM chamber, including the chamber walls and ESEM stage, was carefully cleaned using isopropanol for the third ESEM exposure.

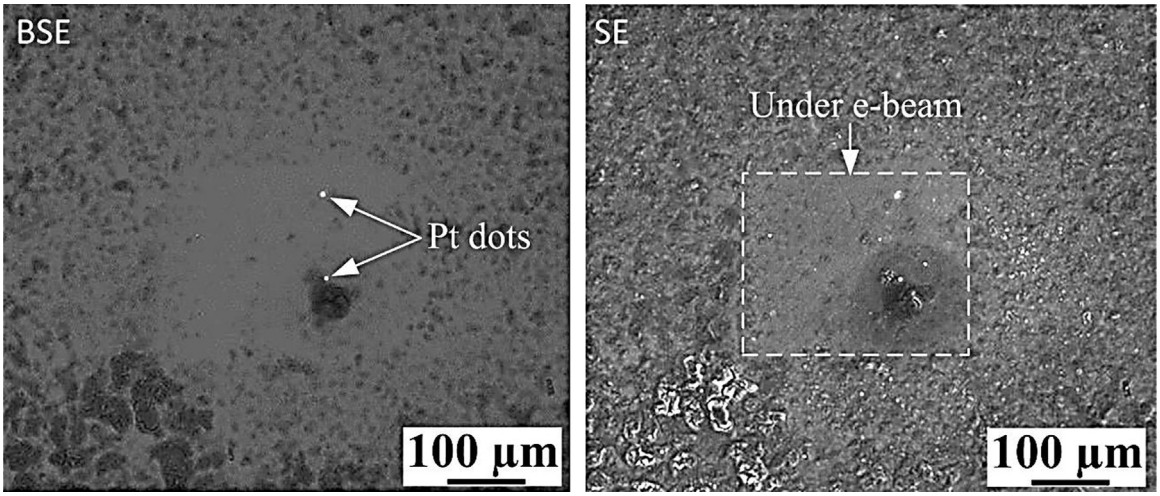

Fig. 5. SE and BSE SEM micrographs from the area exposed by ESEM in-situ and under the e-beam. The e-beam scanned area is visible in both BSE and SE SEM images.

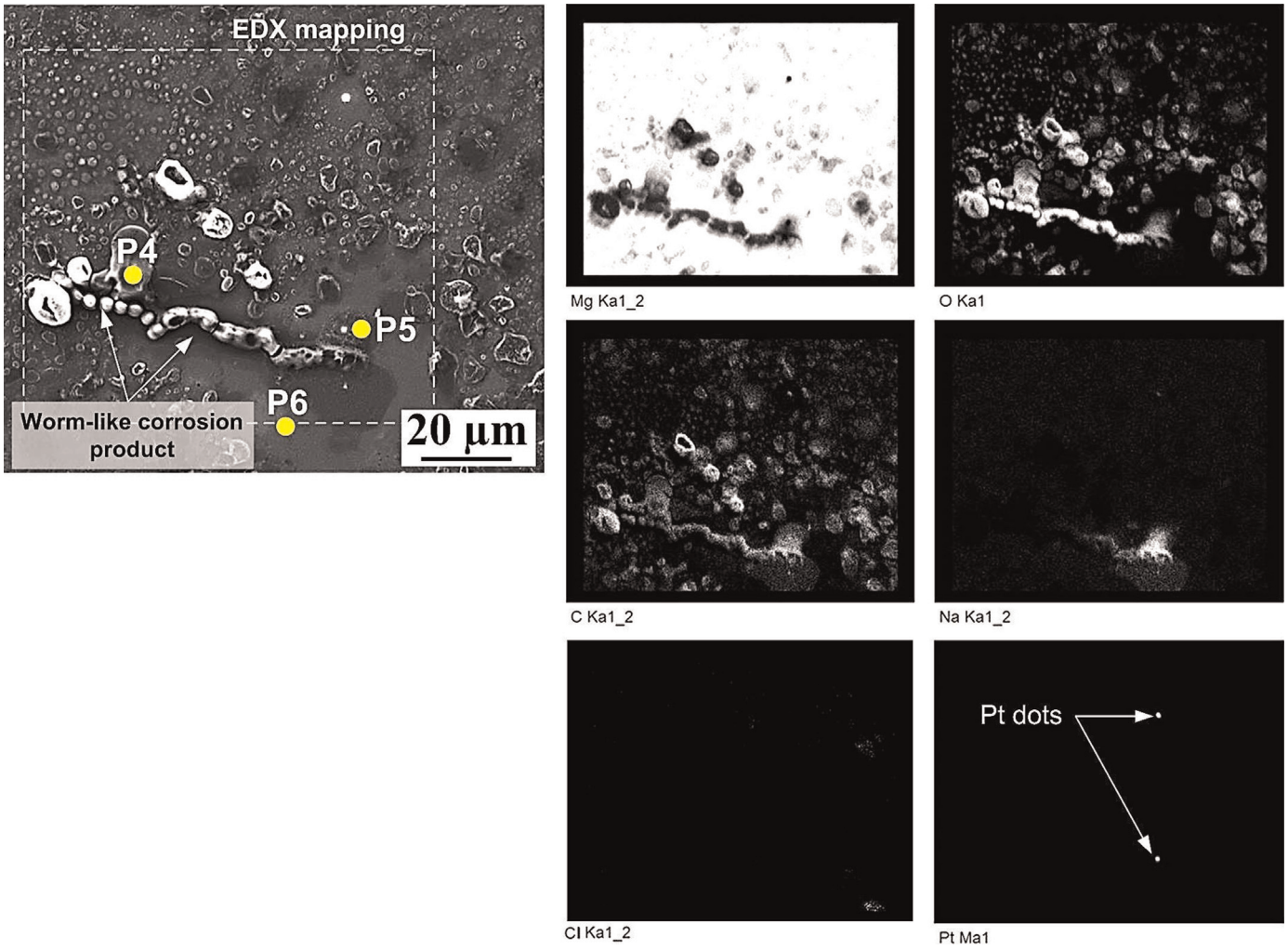

Fig. 6. SEM backscattered electron image and EDX maps on pure Mg exposed by ESEM in-situ from the region that was 4 mm away from the e-beam. The chemical composition of P3, P4 and P5 are listed in Table 2.

Fig. 8 shows the corrosion morphology and EDX point analysis of the third exposure. Similarly to the previous in-situ exposure sample, the scanned area was affected by e-beam, Fig. 8a. The morphology of the corrosion product on this sample can be clearly seen in the high magnification image in Fig. 8b. In this case, the morphology of corrosion crust was almost similar to that of the sample exposed ex-situ, compare Figs. 8b and 7a.

When evaluating the EDX data related to the corrosion products, presented in Fig. 8b, it was noticed that the C content was much less than that of the previous in-situ exposure, and

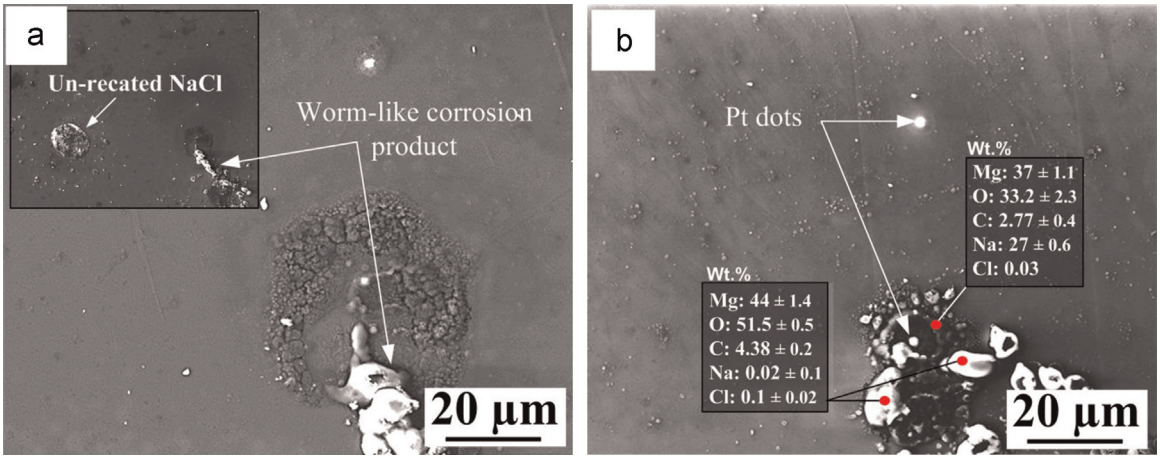

Fig. 7. SEM image and the quantitative EDX analysis on the corrosion product formed on pure Mg exposed ex-situ at 95% RH in a hermetically closed desiccator: (a) region 1 and (b) region 2. Note that there was no difference between the first and the second regions, both contained NaCl particles and Pt dots. The EDX data may be compared with those of sample exposed in ESEM in-situ presented in Table 2.

accordingly chemical compositions of the corrosion crusts were very close to that of the sample exposed ex-situ in the desiccator. This indicated that our hypothesis on the source of high C content was correct.

The other difference between the third (Fig. 8) and second (Fig. 4) in-situ exposed samples was the extent of NaCl-induced atmospheric corrosion attack. Since RH, exposure time, amount of deposited salt and all other exposure parameters were the same, it was rather strange to observe such difference in the extent of corrosion attack. It was found that the crystallographic orientation of the grains might have played a role in the corrosion kinetic of the grains investigated. It is well-known that the crystallographic orientation can affect the corrosion kinetic in metallic materials, including Mg and Mg alloys [29–32]. In the present study, this was examined by evaluating the crystallographic orientation of the grains exposed in the second and third exposures. Fig. 9 shows the difference in the orientation of the grains, which are marked in the standard stereographic triangle. As seen, there is a great difference in the crystallographic orientation of the metal grains investigated in the third and fourth exposures. The examinations show that while Grain 1 (related to the second ESEM experiment) was within 8° of (0001) orientation, the Grain 2 (related to the third ESEM experiment) was within 6° of $(01\bar{1}0)$ orientation. Thus, one can suggest that the faster corrosion kinetic in the former case in comparison with that of the second exposure was partially related to the different crystallographic orientation of the grains.

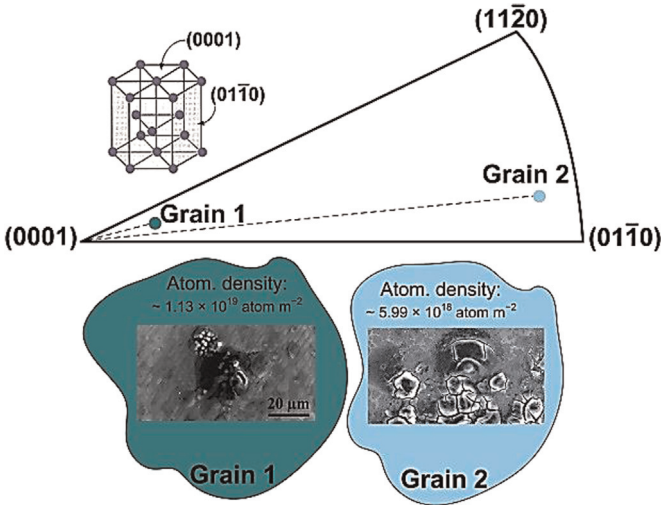

Fig. 9. Crystallographic orientation description of the Grain 1 (the second exposure) and Grain 2 (the third exposure). The orientations are plotted in the standard stereographic triangle as the surface normal.

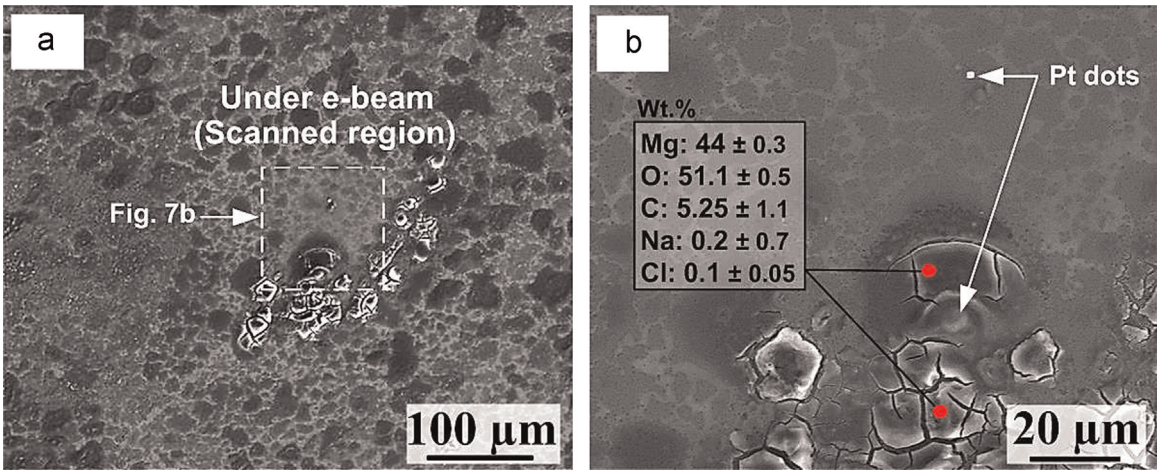

Fig. 8. ESEM micrographs with (a) low and (b) high magnifications as well as the EDX analysis of the corroded pure Mg (the third in-situ exposure). The sample and ESEM chamber were carefully cleaned prior to this exposure. The rectangle shows the affected area by e-beam.

4. Discussion

4.1. The atmospheric corrosion process of Mg

The formation of corrosion product on the location of NaCl (s) illustrates the well-known corrosiveness of NaCl towards Mg and Mg alloys [5–8]. The NaCl added before exposure forms an aqueous solution in the experimental conditions (95% RH), and accordingly an electrolyte film consisting of NaCl(aq) solution is observed on the pure Mg surface in the ESEM in-situ exposures. Therefore, the NaCl-induced atmospheric corrosion processes investigated in this work occur in the presence of small amounts of aqueous solution. Similar to other reactive metals, the stability of Mg and Mg alloys depends on the formation of a surface film, known as passive film, which is capable of preventing corrosion attack when it is exposed to a ambient air. However, the film formed on the surface of Mg and Mg alloys shows poor protective performance in mild to severe corrosive environments and is very prone to breakdown. When exposed to dry air, magnesium oxide, MgO, is rapidly formed (see Eq. (2)) on the metal surface due to high affinity of Mg to oxygen with a thickness of few nanometers. Since MgO, like many other solid corrosion products, is an insulator corrosion product, it diminishes the electronic conductivity and as a result noticeably reduces the corrosion rate.

$$Mg(s)+1/2O_2(g)\rightarrow MgO(s)\ \text{(magnesium oxide)} \quad (2)$$

Pure Mg shows good corrosion resistance in dry air at normal ambient temperature due to the formation of the protective oxide film. however, moisture (humid air or aqueous environments with >1 Ppm H_2O) converts this oxide film to a hydrated oxide, $Mg(OH)_2$, according to the following equation [7]:

$$MgO(s)+H_2O(g)\rightarrow Mg(OH)_2\ \text{(magnesium hydroxide)} \quad (3)$$

In an aqueous solution Mg reacts according to the following electrochemical reactions resulting in the formation of Hydrogen gas and Mg hydroxide:

$$Mg(s)+2H_2O(aq)\rightarrow Mg(OH)_2(s)+H_2(g) \quad (4)$$

$$Mg\rightarrow Mg^{2+}+2e^- \quad (5)$$

$$Mg^{2+}+2OH^-\rightarrow Mg(OH)_2 \quad (6)$$

Hence, corrosion of Mg is expected to be strongly localized in the presence of NaCl(aq). Brucite is an electronic insulator and therefore a poor electrode for the cathodic process. Therefore, the corrosion of Mg is greatly accelerated by cathodically active, impurities of intermetallic prticles containing, e.g., Fe [7,26].

Based on the discussions above and the EDX data (Fig. 7) it is reasonable to conclude that the corrosion products formed on the surface of the pure Mg exposed ex-situ are mainly composed of brucite. This corrosion product is frequently observed on Mg and Mg alloys especially in the CO_2-free environments [5,9]. It may be noted that the laboratory studies on the corrosion behavior of Mg and its alloys in the absence of CO_2 is of importance as it can be illustrative of conditions in crevices and beneath organic coatings where the supply of CO_2 is limited [9].

Concerning the morphology of the corrosion products, it was observed that the corrosion products tend to form elongated worm-like features in some cases, see for e.g. Fig. 7a. Similar observations are reported in [33] for the case of Mg alloy AM50 and pure copper, where it is argued that a high pH develops in droplet boundaries that decreases the surface tension at the electrolyte/oxide interfaces and causes spreading of the electrolyte and droplet coalescence in the absence of CO_2. In contrast, such morphology is in not the case for samples exposed in the presence of ambient levels of CO_2.

The EDX analyses on the sample exposed in the desiccator (the ex-situ exposure) showed that electrolyte layer and ionic species are redistributed on the Mg surface. Among different catalysts, Pt, which was deposited on the metal surface, exhibits extreme electrocatalytic for hydrogen evolution reaction with exceptionally high exchange current density and small Tafel slope [34]. Hence, it is expected that the combination of Pt and Mg leads to a strong galvanic couple and causes the formation of high pH and accordingly the migration of Na cations towards the surrounding regions of Pt dots. Such system may resemble the galvanic corrosion cells that are formed in two-phase magnesium-aluminum (Mg–Al) alloys, where there is micro-galvanic effect of α-Mg and intermetallic β phase particles [35,36]. The scarce evidence for Cl on the regions of anodic sites is an indication of their migration towards the corrosion pits. This has been shown in a recent study [7,35], where Cl was accumulated in the pits and especially in the interface of the corrosion products and metal surface. Thus, one can conclude that Na and Cl ions were migrated towards cathodic and anodic sites, respectively, which is in accordance with the electrochemical nature of NaCl-induced atmospheric corrosion of Mg and Mg alloys.

4.2. The corrosion process inside the ESEM chamber

have been widely studied, see for–>In order to appropriately employ the ESEM technology it is required to fundamentally understand the ESEM technique. During the last two decades, various aspects of the ESEM method such as the evaporation processes inside the instrument chamber and beam transfer characteristics of ESEM have been widely studied, see for e.g. [37–40]. The introduction mentions the successful applications of this technique in different research areas. In the present study, we examined the feasibility of the ESEM method in the corrosion of a pure Mg. Here, we discuss the benefits of the ESEM technique for studying a corrosion process inside an ESEM chamber.

Three different exposures were performed at 4 °C and for 320 min at 75% (the first exposure) and 95% RH (the second and third exposures). These RH values were achieved by a careful control over the temperature and water vapor pressure inside the ESEM chamber. When comparing the corrosion process occurred on the pure Mg at 75% and 95% RH, it was observed that the kinetic of the corrosion was slower in the case of 75% RH as no corrosion crust was observed in the sample exposed in the ESEM at 75% RH that was not the case for the sample exposed at 95% RH. Instead, unreacted NaCl(s) was detected on the sample surface at 75% RH. The required wetting time for conversion of NaCl(s) to the electrolyte film was about 10 and 120 min for the case of 95% and 75% RH, respectively, which showed the slower atmospheric corrosion process at 75% RH. It may be noted that because NaCl absorbs water to form an aqueous solution at RH $>75\%$ in the temperature range studied, it is suggested that the actual RH obtained from the first in-situ experiment is slightly more than 75%. This could happen due to an error of the instrument.

The morphology of the corrosion products formed on the 99.97% Mg was almost the same as the ex-situ exposures. Thus, worm-like corrosion crusts were observed in some regions. Such localized corrosion attack was related the concentration CO_2 that was very low (in range of few ppm) in the instrument chamber. Moreover, the formation of micro-sized corrosion nodules on the metal surface of the ESEM in-situ exposure was similar to that the ex-situ experiment, see Fig. 3b and the ESEM micrograph after 320 min in Fig. 5. The major difference between the in-situ and ex-situ exposure results was found in the chemical composition of the corrosion products; where a significantly higher amount of C content was detected on the second ESEM exposure especially in the region that was under the e-beam for 320 min, see for e.g. P1

in Table 2. This discrepancy deserves future discussions and requires an understanding of the dynamic reactions occurring during the in-situ exposures.

There have been some studies aiming at understand of the effect of factors such as environmental condition and irradiation effect especially on soft or hydrated materials [41,42]. The samples exposed in the ESEM instrument are susceptible to surfaces damages due to (i) the absence of a protective coating on the specimen surface that increase the probability for surface damaging by the electron beam, and (ii) the presence of water vapor that results in the creation of free radicals and other charged species, which known to be a significant reason for radiation damage. The former reason can be described by the collision of electrons with water molecules. Thus, inelastic scattering results in the formation of ionized (Eq. (7)) or excited water (Eq. (8)) molecules:

$$e^- + H_2O \rightarrow H_2O^+ + 2e^- \quad (7)$$

$$e^- + H_2O \rightarrow H_2O^* + e^- \quad (8)$$

Water molecules in the excited state can then decay into free radicals reaction (9) or ions (10):

$$H_2O^* + e^- \rightarrow H. + OH \quad (9)$$

$$H_2O^* + e^- \rightarrow H^+ + OH^- \quad (10)$$

where H^+ is a proton and OH^- is the hydroxy ion. Of these, the OH^- species have a strong affinity to C-containing species such as hydrocarbons inside the ESEM chamber. These may come from the sample or/and silicon oils from the diffusion pump and the grease of vacuum seals and also fingerprints [43]. During the ESEM experiment, it was noticed that some parameters such as accelerating voltage and working distance can exacerbate the irradiation damage during the continuous imaging of the corrosion process. We should also remember that a suitable imaging condition in the ESEM (in the presence of water vapor) can be achieved by a short working distance (4 mm in this work) and a rather high primary energy. Such parameters do increase the irradiation effects [43], and thus there is a tradeoff to be reached.

It was noticed that the C content of the corrosion products were reached almost to that of the sample exposed ex-situ when the ESEM chamber was cleaned by isopropanol and the corrosion coupon was cleaned by plasma cleaning, compare the EDX results presented in Figs. 3 and 8. Therefore, a carful cleaning procedure prior to an ESEM in-situ experiment is an essential prerequisite to produce results that are comparable with the ex-situ exposures. There might be other explanations for the noticeable effect from the e-beam observed (see Figs. 5 and 8) in the scanned regions. Firstly, it is known that some fraction water vapor is ionized due to collision with secondary electrons [1,2]. This can play a role in the corrosion process occurring under e-beam. Besides, the shooting of electrons to the scanned region may affect the electrochemical process by suppressing the anodic reaction (Eq. (5)) to the right and causes a slower NaCl-induced atmospheric corrosion process. Thus, a suggestion that might be useful for getting less C contaminations and performing successful continuous imaging throughout a corrosion process inside the ESEM is that the electron gun should be blanked during exposure and turned on with specific time intervals for the imaging purposes. This for sure will result in much less irradiation damage onto the metal surface, and accordingly less influence to the corrosion process.

Experimental observations in combination with EDX analyses revealed that the extent of corrosion in the third (cleaner) exposure were larger than that of the second exposure, despite all the exposure parameters were the same. By given the fact that CO_2 has an inhibitive effect on the atmospheric corrosion of metals, especially Mg and Mg alloys [5], it can be suggested that the difference in the extent of corrosion can be partially due to the presence of less C content in the third exposure. Besides, the EBSD data provided a clear evidence for the difference in the crystallographic orientation of the individual grains exposed in the second and third exposures. From the literature [30,31], it is reasonable to assume that close packed planes with high atomic packing densities would form a more effective barrier against penetration of chloride ions, resulting in better protection of the magnesium surface. As reported by Cheng et al. [44], the packing of low-index planes for pure Mg show that the atomic density of the planes are in the order $(0001) > (11\bar{2}0) > (01\bar{1}0)$. Thus, there is a strong corrosion dependence on crystallographic orientation of pure Mg. The results showed that the grains exposed in the second and third exposure had a crystallographic orientation very close to (0001) and $(01\bar{1}0)$ orientations, respectively. Hence, the more severe corrosion attack in the third exposure can also be attributed to the differences in their crystallographic orientation.

5. Conclusion

The capability of ESEM in studying the NaCl-induced atmospheric corrosion of 99.97% Mg was examined by comparing the results with those of an ex-situ exposure. The main conclusions drawn from this study are as follows:

- The morphology of the corrosion products formed during an ESEM in-situ exposure is comparable with that of the ex-situ exposure.
- The composition of corrosion products, however, was strongly effected by carbon contaminations present inside the ESEM chamber as well as on the sample surfaces.
- It was shown that a proper cleaning procedure of the instrument chamber by isopropanol and the sample by plasma cleaning can greatly reduce the carbon contaminations and thus make an in-situ experiment comparable to the ex-situ exposures.
- A strong effect of e-beam on the corrosion process of Mg was observed. This was attributed to the carbon contaminations and also the difference in the crystallographic orientation of grains. It was suggested that the beam gun should be blanked during exposure and turned on with specific time intervals for the imaging purposes to minimize this effect.
- It was also noticed that, although the kinetic of the corrosion process is affected by electron beam; the composition of the corrosion products is not.

References

[1] G.D. Danilatos, J. Microsc. 162 (1991) 391.
[2] A. Jansson, A. Nafari, A. Sanz-Velasco, K. Svensson, S. Gustafsson, A. M. Hermansson, E. Olsson, Microsc. Microanal. 19 (2013) 30.
[3] G.D. Danilatos, Microsc. Res. Technol. 25 (1993) 354.
[4] M. Jönsson, D. Persson, C. Leygraf, Corros. Sci. 50 (2008) 1406.
[5] M. Shahabi-Navid, M. Esmaily, J.E. Svensson, M. Halvarsson, L. Nyborg, Y. Cao, L.G. Johansson, J. Electrochem. Soc. 161 (2014) C277.
[6] L. Yang, Y. Li, Y. Wei, L. Hou, Y. Tian, Corros. Sci. 52 (2010) 2188.
[7] G. Song, A. Atrens, Adv. Eng. Mater. **5** (2003) 837.
[8] Y.G. Li, Y.H. Wei, L.F. Hou, P.J. Han, Corros. Sci. 69 (2013) 67.
[9] M. Esmaily, M. Shahabi-Navid, J.E. Svensson, M. Halvarsson, L. Nyborg, Y. Cao, L.G. Johansson (in press), Corros. Sci. (2015).
[10] J. Chen, J.Q. Wang, E.H. Han, W. Ke, Corr. Eng. Sci. Technol. 46 (2011) 267.
[11] T.J. Chen, X.D. Jiang, Y. Ma, Y.D. Li, Y. Hao, J. Alloy. Compd. 505 (2010) 476.
[12] J. Chen, J. Wang, E. Han, W. Ke, Electrochem. Commun. 10 (2008) 577.
[13] J. Chen, J. Wang, E. Han, W. Ke, Corros. Sci. 50 (2008) 2338.
[14] J. Chen, J. Wang, E. Han, W. Ke, Corros. Sci. 51 (2009) 477.
[15] J. Chen, J. Wang, E. Han, W. Ke, Corros. Sci. 49 (2007) 1625.
[16] S. Rossi, M. Fedel, F. Deflorian, Mater. Corros. 65 (2012) 466.

[17] B. Pöter, I. Parezanovic, M. Spiegel, Mater. High Temp. 22 (2005) 9.
[18] B. Schmid, N. Aas, O. Grong, R. Odegård, Oxid. Met. 57 (2002) 115.
[19] P. Bruckel, P. Lours, P. Lamesie, B. Pieraggi, Mater. High Temp. 20 (2003) 551.
[20] T. Jonsson, B. Pujilaksono, S. Hallström, J. Ågren, J.E. Svensson, L.G. Johansson, M. Halvarsson, Corros. Sci. 51 (2009) 1914.
[21] M. Jönsson, D. Persson, D. Thierry, Corros. Sci. 49 (2007) 1540.
[22] Z. Cui, X. Li, K. Xiao, C. Dong, Corros. Sci. 76 (2013) 243.
[23] J. Liao, M. Hotta, S. Motoda, T. Shinohara, Corros. Sci. 71 (2013) 53.
[24] L. Yang, Y. Li, Y. Wei, L. Hou, Y. Tian, Corros. Sci. 52 (2010) 2188.
[25] Y.G. Li, Y.H. Wei, L.F. Hou, P.J. Han, Corros. Sci. 69 (2013) 67.
[26] M. Jönsson, D. Thierry, N. LeBozecb, Corros. Sci. 48 (2006) 1193.
[27] M. Esmaily, M. Shahabi-Navid, N. Mortazavi, J.E. Svensson, M. Halvarsson, M. Wessén, A.E.W. Jarfors, L.G. Johansson, Mater. Charact. 95 (2014) 50.
[28] J. Balej, Int. J. Hydrog. Energy 10 (1985) 233.
[29] B.J. Wang, D.K. Xu, J.H. Dong, W. Ke, Scr. Mater. 88 (2014) 5.
[30] G. Song, R. Mishra, Z. Xu, Electrochem. Commun. 12 (2010) 1009.
[31] G. Song, Z. Xu, Corros. Sci. 54 (2012) 97.
[32] G.L. Song, Z.Q. Xu, Corros. Sci. 63 (2012) 100.
[33] Z.Y. Chen, D. Persson, A. Nazarov, S. Zakipour, D. Thierry, C. Leygraf, J. Electrochem. Soc. 152 (2005) B342.
[34] Y. Zheng, Y. Jiao, M. Jaroniec, S.Z. Qiao, Angew. Mineral. 53 (2014) 2.
[35] M. Esmaily, M. Strom, J.E. Svensson, M. Halvarsson, L.G. Johansson (in press), Corrosion (2015).
[36] M. Esmaily, N. Mortazavi, M. Shahabi-Navid, J.E. Svenssona, M. Halvarsson, L. Nyborg, M. Wessén, A.E.W. Jarfors, L.G. Johansson, J. Electrochem. Soc. 162 (2015) C85.
[37] R.E. Cameron, A.M. Donald, J. Microsc. 173 (1994) 227.
[38] G.D. Danilatos, J. Rattenberger, V. Dracopoulos, J. Microsc. 242 (2011) 166.
[39] G.D. Danilatos, J. Microsc. 242 (2011) 159.
[40] G.D. Danilatos, Micron 44 (2013) 143.
[41] R.E. Cameron, A.M. Donald, J. Microsc. 173 (1994) 227.
[42] C. Gilpin, D.C. Sigee, J. Microsc. 179 (1995) 22.
[43] D.J. Stokes, Philos. Soc. 361 (2003) 2771.
[44] G. Chang, S. Chen, Q. Li, X. Yue, Y. Qi, Int. J. Min. Metall. Mater. 19 (2012) 136.